METALLURGY

Ultrahigh-strength and ductile superlattice alloys with nanoscale disordered interfaces

T. Yang[1,2]*, Y. L. Zhao[1,3]*, W. P. Li[3], C. Y. Yu[4], J. H. Luan[3], D. Y. Lin[5], L. Fan[6], Z. B. Jiao[6], W. H. Liu[7], X. J. Liu[7,8], J. J. Kai[1,3], J. C. Huang[2,3], C. T. Liu[1,2,3]†

Alloys that have high strengths at high temperatures are crucial for a variety of important industries including aerospace. Alloys with ordered superlattice structures are attractive for this purpose but generally suffer from poor ductility and rapid grain coarsening. We discovered that nanoscale disordered interfaces can effectively overcome these problems. Interfacial disordering is driven by multielement cosegregation that creates a distinctive nanolayer between adjacent micrometer-scale superlattice grains. This nanolayer acts as a sustainable ductilizing source, which prevents brittle intergranular fractures by enhancing dislocation mobilities. Our superlattice materials have ultrahigh strengths of 1.6 gigapascals with tensile ductilities of 25% at ambient temperature. Simultaneously, we achieved negligible grain coarsening with exceptional softening resistance at elevated temperatures. Designing similar nanolayers may open a pathway for further optimization of alloy properties.

Alloys with atomically close-packed ordered structures constitute a class of structural materials that bridge the gap between ordinary metals and hard ceramics, with potentially novel mechanical properties (*1*–*3*). These long-range ordered superlattice alloys have strong chemical binding and associated low atomic mobility, which make them very attractive to high-temperature structural applications for achieving increased energy efficiencies in a wide range of engineering fields, such as aerospace, automotive, gas turbine engine, and many other industries (*4*–*6*). Since the 1950s, considerable efforts have been devoted to the research and development of bulk ordered alloys. Despite many advances that have been made, widespread application of these alloys remains elusive, largely limited by the irreconcilable conflict between strength and ductility at ambient temperatures. As the crystalline structure of alloys becomes highly ordered, catastrophic brittle failure takes place easily at ambient temperatures and demolishes the most desirable properties of the alloys. Consequently, most conventional ordered alloys with ultrahigh strengths (gigapascal levels) are found to be extremely brittle during tensile deformation, which severely limits their potential use in structural applications. For example, alloys with the topologically close-packed (TCP) structure (e.g., the Laves-phase ordered alloys) offer appreciable strengths (or hardnesses) at elevated temperatures, but their insufficient number of operating slip systems allows for negligible tensile elongations (*5*, *7*). A respectable ductility exists in a few cubic ordered alloys (*8*–*13*), such as binary Ni_3Al, FeAl, and NiAl aluminides. However, their yield strengths remain quite limited at ambient temperatures, and they are insufficiently strong for use in many engineering fields. Furthermore, a lack of sufficient thermal stability at elevated temperatures is another concern for their practical usage. Alloys in their polycrystalline forms are generally unstable at high temperatures. Thermally driven structural instability, such as rapid or abnormal grain coarsening and associated softening behaviors, poses a severe limitation on their use at elevated temperatures. One solution is to grow large single crystals to solve this problem; however, this technique requires a set of extremely complicated processes with high manufacturing costs and a long production cycle.

We departed from the traditional high-temperature alloy design strategy by focusing on nanoscale interfacial disordering. This presents a different direction for tuning the microstructures through synergistic modulations of structural and chemical features of bulk ordered alloys to target superb mechanical properties and exceptional thermal stability. By controllably incorporating multiple elements, we synthesized a $Ni_{43.9}Co_{22.4}Fe_{8.8}Al_{10.7}Ti_{11.7}B_{2.5}$ [in atomic percentage (at %)] alloy by using arc melting and thermomechanical processing (*14*). The superlattice materials (SMs) that we developed have nanoscale disordered interfaces (NDI-SMs) with a polycrystalline morphology (11.0 ± 7.5 μm average grain size) with an unusual structural feature composed of the micrometer-scale ordered superlattice grain (OSG) capsulated with a disordered interfacial nanolayer (DINL). The $L1_2$-type ordered structure (a close-packed A_3B-type ordered structure) of the grain interior was identified using bright-field transmission electron microscopy (TEM) (Fig. 1A).We conducted aberration-corrected high-angle annular dark-field scanning transmission electron microscopy (HAADF-STEM) analyses to probe the detailed atomic structures and chemistries (Fig. 1, B to D). The inner grain exhibits a highly $L1_2$-type chemical ordering with distinct atomic complexities of the constituent sublattices. We used atomic-resolution energy-dispersive x-ray spectroscopy (EDX) mapping (Fig. 1B) to show that Ti and Al atoms mainly occupy the vertices (B sublattice) of the $L1_2$ unit cell, whereas the faced centers (A sublattice) are occupied mainly by Ni and Co atoms. Iron atoms occupy both the sublattice sites of the $L1_2$ unit cell and allow the alloy to be stoichiometric. This sorting of the complex atomic site-occupation behavior is remarkably different from that of conventional binary ordered alloys, in which each sublattice is essentially occupied by a single type of element (fig. S1). Partial replacement of Ni with Fe and Co decreases the electron density (the average number of electrons per atom outside the inert gas shell) of the ordered structure. This structure helps suppress the formation of brittle hexagonal or tetragonal ordered phases (*15*). We also can clearly identify a distinctive interfacial disordering. This creates an ultrathin disordered layer (~5 nm in thickness) along the grain boundary with a face-centered cubic (fcc) solid-solution structure (Fig. 1C). The volume fraction of interfacial disordered nanolayer can be estimated to be ~0.13% (*14*). We found that this disordered nanolayer is highly coherent with that of the host ordered grain with a small lattice mismatch of ~0.2% (*14*). Moreover, we found that the Fe and Co atoms show a strong tendency to segregate at the boundary regions, whereas the Ni, Al, and Ti atoms are largely depleted (Fig. 1D). This distinctive interfacially disordered superlattice structure (Fig. 1E) is substantially different from that of conventional ordered alloys reported previously.

We used three-dimensional atom probe tomography (3D-APT) to provide a quantitative compositional analysis at the atomic scale. This technique is especially important to quantify the light element boron (Fig. 2A). The $L1_2$-type ordered superlattice of the grain interior is compositionally homogeneous without elemental clustering. We identified it as the $(Ni,Co,Fe)_3(Al,Ti,Fe)$-type compositionally complex ordered superlattice with a small amount of boron occupying the interstitial positions (*16*). By contrast, we found that the Fe and Co are strongly enriched inside the DINL accompanied with codepletion of Ni, Al, and Ti elements, which is consistent with our TEM analyses. We were also able to clearly identify local boron enrichment within the DINL with 3D-APT, as EDX is not capable of accurately determining

[1]Department of Mechanical Engineering, City University of Hong Kong, Hong Kong, China. [2]Hong Kong Institute for Advanced Study, City University of Hong Kong, Hong Kong, China. [3]Department of Materials Science and Engineering, City University of Hong Kong, Hong Kong, China. [4]College of Physics and Optoelectronic Engineering, Shenzhen University, Shenzhen, China. [5]Software Center for High Performance Numerical Simulation and Institute of Applied Physics and Computational Mathematics, Chinese Academy of Engineering Physics, Beijing, China. [6]Department of Mechanical Engineering, The Hong Kong Polytechnic University, Hong Kong, China. [7]School of Materials Science and Engineering, Harbin Institute of Technology, Shenzhen, China. [8]Institute of Materials Genome and Big Data, Harbin Institute of Technology, Shenzhen, China.
*These authors contributed equally to this work.
†Corresponding author. Email: chainliu@cityu.edu.hk

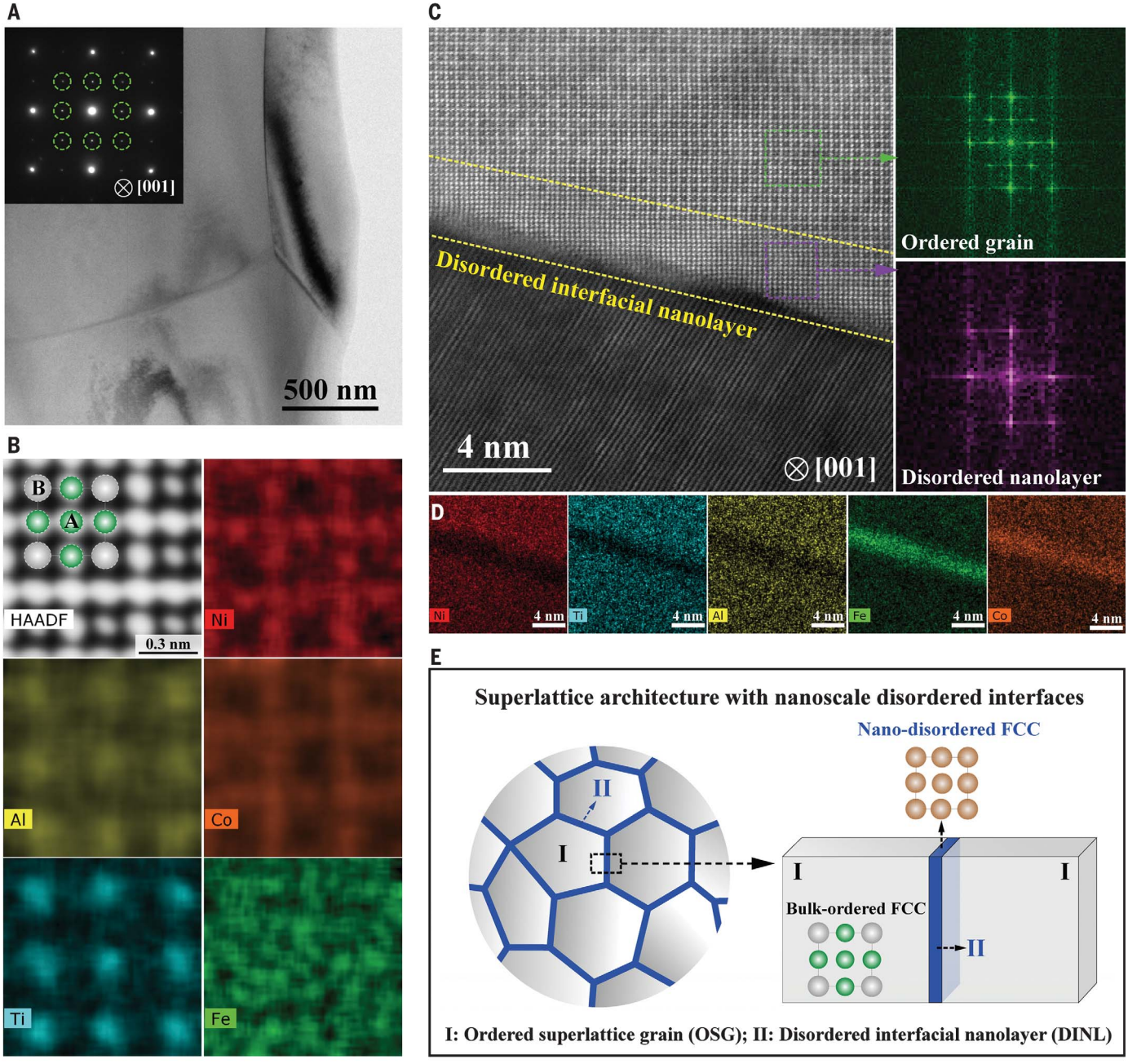

Fig. 1. Unusual nanoscale interfacially disordered structure of the superlattice materials. (**A**) Bright-field TEM image showing the polycrystalline morphology. (Inset) A corresponding selected-area electron diffraction pattern collected from the grain interior, which shows the $L1_2$-type ordered structure. (**B**) Atomic-resolution HAADF-STEM image and corresponding EDX maps taken from the inner $L1_2$-type OSG, revealing the sublattice occupations. (**C**) High-resolution HAADF-STEM image revealing the ultrathin disordered layer at the grain boundaries with a nanoscale thickness. The images on the right show the corresponding fast Fourier transform (FFT) patterns. (**D**) EDX maps showing the compositional distribution of the DINL. (**E**) Schematic illustration highlighting the nanoscale interfacially disordered structure. FCC, face-centered cubic.

the boron locations. Two-dimensional compositional contour maps across the interface revealed a distinctive multielement cosegregation of Fe, Co, and B inside the DINL (Fig. 2B). The one-dimensional compositional profile revealed the quantitative elemental partitioning of each element (Fig. 2C). We found that large amounts of Fe (from 8.92 ± 0.32 to 20.04 ± 0.41 at %) and Co (from 22.36 ± 0.47 to 30.69 ± 0.47 at %) were segregated strongly to the DINL compared with the inner OSG. We also detected a slight enrichment of boron (from 1.15 ± 0.12 to 2.11 ± 0.15 at %). Evidently, the multielement cosegregation plays a decisive role in the nanoscale interfacial disordering.

We constructed a corresponding supercell using density functional theory (DFT) calculations to help visualize this chemically complex superlattice (fig. S2). We evaluated the effect of small amounts of boron on the ordering energy, which has a negligible impact on the disordering of this complex $L1_2$-type superlattice (fig. S3). Chiba *et al.* (*17*, *18*) have demonstrated that additions of fcc formers to the Ni_3Al alloy that prefer to substitute for the Ni sublattice, like Fe and Co, promote the fcc-type disordering by reducing the alloy's ordering degree. Collectively, we attribute the nanoscale interfacial disordering in our NDI-SMs mainly to the substantial cosegregation of Fe and Co

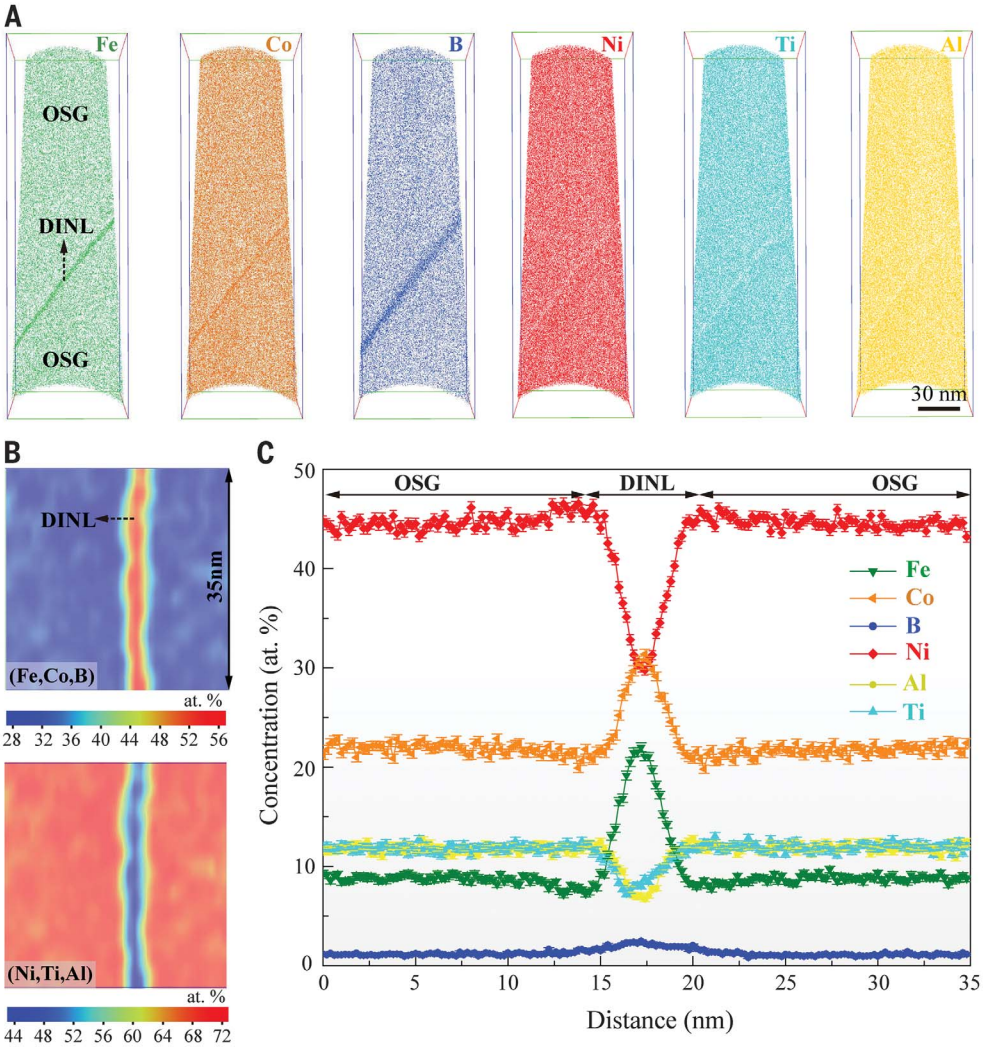

Fig. 2. Three-dimensional compositional distributions and nanoscale interfacial cosegregation of the NDI-SMs. (**A**) Atom maps reconstructed using 3D-APT that show the distribution of each element. Fe, Co, and B are enriched at the DINL, whereas Ni, Al, and Ti are depleted correspondingly. (**B**) Two-dimensional compositional contour maps revealing the multielement cosegregation behaviors of Fe, Co, and B elements within the DINL. (**C**) One-dimensional compositional profile that quantitatively reveals the elemental distributions across the OSG and DINL.

at the grain boundaries. Moreover, given the chemically complex nature, containing multiple principal elements, the DINL can be regarded as an fcc-type disordered high-entropy nanolayer, which itself is extremely ductile with excellent work-hardening capability under the tensile deformation (*19*, *20*). With the formation of this ductile DINL, the intergranular embrittlement—one major concern for bulk polycrystal ordered alloys—seems to be virtually eliminated in our alloy.

Leveraging on this nanoscale interfacially disordered structure, we achieved a superior strength-ductility synergy in the NDI-SM at ambient temperature (Fig. 3 and table S1). The NDI-SM has an ultrahigh yield strength (σ_y) of ~1040 ± 61 MPa (Fig. 3A), which is ~2.6 times as strong as that of the binary Ni_3Al alloy (~320 MPa) with a similar grain size (*21*). The NDI-SM has a large tensile elongation of 25 ± 1%, a distinct departure from conventional high-strength bulk ordered alloys that are generally very brittle at room temperature. Furthermore, the NDI-SM has a pronounced work-hardening capability, reaching an ultimate tensile strength (σ_{uts}) of ~1611 ± 2 MPa. Moreover, we observed numerous dimpled structures on the fracture surface (inset in Fig. 3A). These structures are characteristic of ductile fracture mode and show the inherently ductile nature and plastic deformability of the NDI-SM. We directly compare these properties with those of conventional high-performance bulk ordered alloys (*8*–*10*, *12*, *13*, *17*, *18*, *22*–*26*), thereby demonstrating the singular combination of high strength and large ductility of this alloy, as indicated in Fig. 3B.

We measured the variations of hardness and grain size to evaluate thermal responses of our as-prepared NDI-SM at elevated temperatures. We found a better resistance to thermal softening as compared with that of other conventional high-temperature ordered alloys from 20 to 800°C (*27*, *28*) (Fig. 3C). We measured a hardness of 417 ± 8 HV (Vickers hardness) at room temperature and a hardness of 392 ± 3 HV at 800°C. We did not observe the onset of obvious softening behavior within this temperature range. Notably, we also discovered an extremely sluggish grain growth over long-duration annealing (up to 120 hours) at a high temperature of 1050°C (Fig. 3D). Most traditional structural materials tend to coarsen rapidly at these temperatures (fig. S4) (*29*–*32*). By contrast, the NDI-SM retains a uniform grain size distribution with almost negligible coarsening (13.1 ± 9.4 μm on average). Moreover, an appreciable strength can still be maintained when tested at a high temperature of 1000°C (fig. S5). We believe that these initial high-temperature observations suggest a high thermal stability of our NDI-SM, which may render this type of alloy specifically suitable for high-temperature structural applications.

We attribute the ultrahigh yield strength of our NDI-SM mainly to the high antiphase boundary (APB) energy of the highly ordered superlattice grain, which produces a strong barrier against both the nucleation and motion of dislocations. Previous studies have suggested that in the ordered Ni_3Al alloy, the

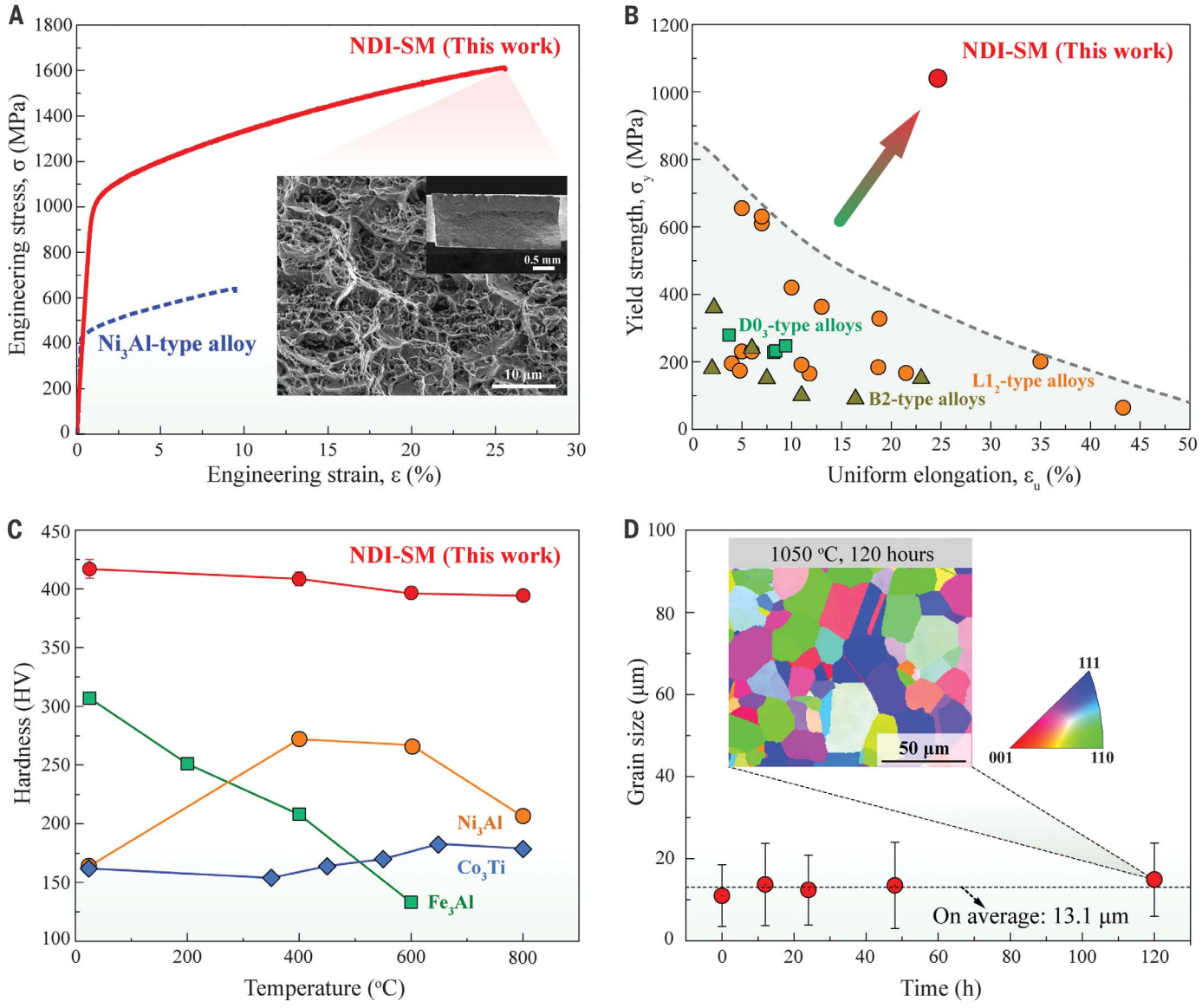

Fig. 3. Mechanical properties and thermal stability of the NDI-SMs. (**A**) Tensile stress-strain curve of the NDI-SM tested at 20°C in air. The stress-strain curve of high-strength Ni_3Al-type (Ni_3Al-2.5 at % B) alloy (*9*) is also plotted for a direct comparison. (Inset) Tensile fractography showing the ductile dimpled structures. (**B**) Yield strength (σ_y) versus uniform elongation (ε_u) of the present NDI-SM compared with various conventional bulk ordered alloys (*8*–*10*, *12*, *13*, *17*, *18*, *22*–*26*). (**C**) Variations of Vickers hardness (HV) of the NDI-SM at elevated temperatures compared with those of conventional ordered alloys (*27*, *28*). (**D**) Grain size variations as a function of heating durations at a high temperature of 1050°C. (Inset) A typical EBSD inverse pole figure (IPF) map showing the grain size of the sample annealed at 1050°C for 120 hours. The NDI-SMs exhibit an exceptionally high resistance against the thermally driven softening and grain coarsening.

addition of Fe and Co that prefer to occupy the Ni or both sublattices has a very small effect on the APB energy (*33*, *34*). A small amount of boron also had a limited effect (*35*). However, Ti occupies the Al sublattice and increases the APB energy substantially (*33*, *34*). We used a model proposed by Crudden *et al.* (*36*, *37*) to estimate the APB energy of ~296 mJ/m^2 for our ordered superlattice. This energy is much higher than that observed in the Ni_3Al alloy (~110 mJ/m^2) (*38*). Theoretically, the macroscopic flow stress of $L1_2$-type ordered superlattices at room temperature is mainly dominated by the process of bowing out of the leading dislocation against the APB (*39*, *40*). The critical shear stress (τ) for dislocation nucleation is found to have a positive correlation with the APB energy (γ); in other words, $\tau = \gamma/\mathbf{b}$, where **b** is the Burgers vector of the ½[110] dislocation (~0.256 nm for the NDI-SM). We can estimate the local shear stress for dislocation nucleation in the OSG as ~722 MPa higher than that in the Ni_3Al alloy. This difference results in a substantial increase of the yield strength. Separately, the presence of interstitial boron atoms further produces an increased lattice resistance to dislocation motion, contributing to the yield strength (*41*).

The large tensile ductility and ductile fracture behavior we observed is primarily caused by the unusual nanoscale interfacial disordering. The disordering plays a crucial role in determining the plastic deformation capability of the NDI-SMs at a high-strength level. Achieving a high tensile ductility is extremely difficult in the bulk polycrystal $L1_2$-type alloys at room temperature, especially under ultrahigh strengths. The usual brittleness is generally ascribed to the poor cohesive strength of grain boundaries, which causes a serious intergranular failure during tensile deformation (*42*). On the basis of this consideration, traditional

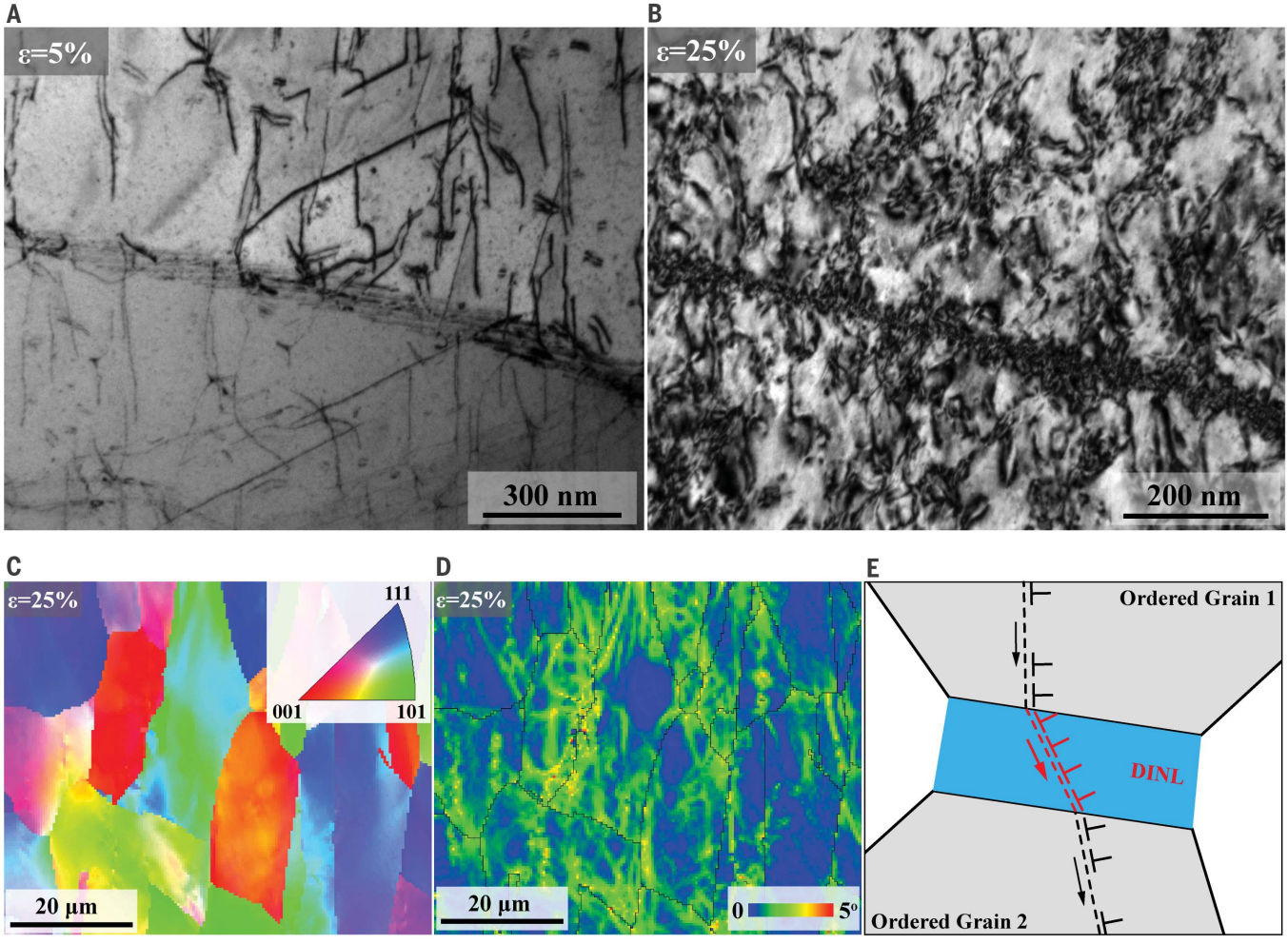

Fig. 4. Plastic deformation micromechanisms and interfacial disordering ductilization. (**A** and **B**) TEM images of the plastically deformed specimens under various tensile strains at room temperature, showing that pronounced dislocation activities can be steadily accommodated at the vicinity of the DINL without intergranular cracks. (**C**) EBSD IPF map. (**D**) Corresponding kernel average misorientation map taken from the fractured specimen, which shows the obvious grain misorientations and pronounced dislocation activities. (**E**) Schematic illustration showing the remarkable ductilization response dominated by the nanoscale interfacial disordering. The DINL serves as a ductile buffer zone between adjacent ordered grains, which enables excellent plastic-deformation compatibility by enhancing dislocation mobilities at grain boundaries, and thus results in the large tensile ductility at an ultrahigh-strength level.

approaches to overcoming embrittlement have been based on enhancing the grain-boundary cohesion.

The boron-doped Ni_3Al alloy is a classic example of this approach. Adding trace amounts of boron (typically 0.1 to 0.5 at %) substantially improves the ductility of polycrystal Ni_3Al (24 at % Al), which tends to segregate at grain boundaries and enhances their cohesive strengths. This allows the alloy to reach a ductility maximum of ~35% at room temperature with 0.5 at % boron doping (*9*). We used TEM characterizations to find a completely ordered structure from the grain interior to the vicinity of the grain boundaries in this boron-doped Ni_3Al alloy (fig. S6). It verifies that the ductilization originates from improved interfacial cohesion rather than the disordering, which is consistent with previous studies (*42*, *43*). Unfortunately, although this toughening strategy has proved to be effective in low-strength ordered alloys, it has been far less effective in high–yield strength alloys. This is particularly true for those with high APB energies (*44*). To see whether the mechanism of increased grain-boundary cohesion could explain our observations, we prepared our NiCoFeAlTi alloy with 0.5 at % of boron. Although we can clearly identify elemental segregation of boron at the interfaces (fig. S7), we found no indication of local disordering at the grain boundaries (fig. S8). In strong contrast to the boron-doped Ni_3Al counterpart with a large ductility, this alloy fractured mechanically within the elastic region, exhibiting a near-zero tensile elongation associated with a serious brittle intergranular fracture (fig. S9). By further increasing the boron concentration to 2.5 at %, we obtained interfacial disordering at the nanoscale from the substantially enhanced multielement cosegregation behavior. The disordered nanolayer was especially effective in suppressing the intergranular fracture, leading to a distinct brittle-to-ductile transition with a large tensile ductility (Fig. 3). The addition of boron plays an important role in promoting the plastic deformability of our NDI-SMs, but the underlying mechanism is distinct and fundamentally different from when it is used for increasing grain-boundary cohesion. Although the addition of a limited amount of boron alone has almost no effect on the disordering of the ordered $L1_2$ structure, a slight increase of boron segregation results in a notable coenrichment of Fe and Co atoms (from 41.24 to 50.73 at % in total) to the interfaces (table S2) and nanoscale disordering at the grain boundaries. To avoid the possible damages of excessive boride, the optimum

level of boron for interfacial disordering in these NDI-SMs was determined to be ~1.5 to 2.5 at % (figs. S10 and S11). This interfacial disordered nanolayer eventually serves as a new route for grain-boundary toughening and enables a steady plastic deformation even under such a high-strength condition.

We carefully characterized the microstructural evolutions near the grain boundaries of the samples after tensile tests, using TEM observations to further identify the deformation micromechanisms. We observed that massive dislocations were operative in the vicinity of the DINL without intergranular cracking (Fig. 4, A and B). The electron backscatter diffraction (EBSD) image taken from the fractured sample (Fig. 4, C and D) shows a clear grain misorientation, which indicates pronounced dislocation activities during the tensile deformation. An important benefit of the nanoscale interfacial disordering, which contributes to the excellent ductility of our NDI-SM even at such a high-strength level, is the enhancement of dislocation mobilities within and across the intrinsically ductile disordered nanolayer (Fig. 4E). More specifically, with the grain-boundary disordering, the strong APB barrier to the nucleation of dislocations is eliminated in the disordered region. This substantially reduces the critical stress for dislocation generation and transmission to a stress level lower than that required for intergranular fracture. Meanwhile, the localized stress imposed on the interfaces is relieved from the grain–boundary disordered sources. During plastic deformation, a large number of dislocations can be dynamically and steadily accommodated at grain boundaries. As a result, with the introduction of this ductile buffer nanolayer, the plastic deformation compatibility between adjacent ordered grains is greatly improved, and the microcrack initiation along such boundaries is effectively suppressed. Hack *et al.* have suggested that, for the ordered superlattice with a high APB energy, an additional energy barrier (generally given as $\pi r^2\gamma/2$, where r is the dislocation loop radius) is required for the emission of dislocation from a crack tip (*44*, *45*). After the disordering of the interfaces, such a strong obstacle is essentially removed and the local stress intensity at the crack tip is reduced accordingly, which leads to much less susceptibility to the propagation of cracks at the interfaces. Taken together, the presence of the DINL increases the failure resistance of grain boundaries, thereby preventing premature fracture of our NDI-SMs. This results in a large tensile ductility coincident with a pronounced work-hardening capability.

We also believe that the DINL is pivotal in suppressing thermally driven grain coarsening. The stabilization mechanism can be interpreted both thermodynamically and kinetically. For most polycrystal materials, grain boundaries generally have a high energy level, and there is a thermodynamic driving force to reduce the area of grain boundaries through grain coarsening. In the present NDI-SMs, the inherent multielement mixing within the DINL substantially increases the configurational entropy and lowers the Gibbs energy of grain boundaries, which effectively reduces the driving force for grain growth (*46*, *47*). Moreover, grain-boundary migration in a duplex system is a consequence of competition between the interfacial disordered nanolayer and the bulk ordered grains, which requires cooperative and collective diffusion of all constituent elements. A negligible increase of grain size after long-term annealing implies that the DINLs in the NDI-SMs are thermally stable at elevated temperatures, with a balanced energy state between the neighboring ordered grains. Because of the solid solubility limit of an individual region, the resulting elemental diffusion between them and the associated grain-boundary motion will be strongly restricted. Concurrently, the local enrichment of multiple elements at grain boundaries may also give rise to a kinetic stabilization of grains owing to the solute-drag effect (*48*, *49*).

The composite architecture of our superlattice alloy, especially the multielement cosegregation-induced interfacial disordering, can be utilized to design high-strength ultrafine-grained or nano-grained materials with enhanced grain-boundary stability and associated coarsening resistance. We anticipate that this approach should be applicable to many other metallic systems, particularly the compositionally complex ordered alloys. This may lead to families of high-temperature structural materials that might avoid some of the drawbacks of high-temperature alloys currently in use. These superlattice materials will be of great interest for a broad range of aerospace, automotive, nuclear power, chemical engineering, and other applications.

REFERENCES AND NOTES

1. C. T. Liu, R. W. Cahn, G. Sauthoff, Eds., *Ordered Intermetallics: Physical Metallurgy and Mechanical Behaviour*, vol. 213 of *NATO Science Series* (Springer, 2012).
2. M. Armbrüster *et al.*, *Nat. Mater.* **11**, 690–693 (2012).
3. R. W. Cahn, *Contemp. Phys.* **42**, 365–375 (2001).
4. D. P. Pope, *MRS Proceedings* **81**, 3 (1986).
5. R. L. Fleischer, R. J. Zabala, *Metall. Trans. A* **21**, 2709–2715 (1990).
6. J. A. Lemberg *et al.*, *Intermetallics* **20**, 141–154 (2012).
7. C. T. Liu, J. H. Zhu, M. P. Brady, C. G. McKamey, L. M. Pike, *Intermetallics* **8**, 1119–1129 (2000).
8. C. G. McKamey, J. H. DeVan, P. F. Tortorelli, V. K. Sikka, *J. Mater. Res.* **6**, 1779–1805 (2011).
9. K. Aoki, *Mater. Trans. JIM* **31**, 443–448 (1990).
10. J. D. Cotton, R. D. Noebe, M. J. Kaufman, *Intermetallics* **1**, 3–20 (1993).
11. K. Gschneidner Jr. *et al.*, *Nat. Mater.* **2**, 587–591 (2003).
12. T. Yamaguchi, Y. Kaneno, T. Takasugi, *Scr. Mater.* **52**, 39–44 (2005).
13. C. T. Liu, E. H. Lee, C. G. McKamey, *Scr. Metall.* **23**, 875–880 (1989).
14. Materials and methods are available as supplementary materials.
15. C. T. Liu, H. Inouye, *Metall. Trans. A* **10**, 1515–1525 (1979).
16. S. N. Sun, N. Kioussis, S.-P. Lim, A. Gonis, W. H. Gourdin, *Phys. Rev. B* **52**, 14421–14430 (1995).
17. A. Chiba, S. Hanada, S. Watanabe, *Acta Metall. Mater.* **39**, 1799–1805 (1991).
18. A. Chiba, S. Hanada, S. Watanabe, in *High Temperature Aluminides and Intermetallics*, S. H. Whang, D. P. Pope, C. T. Liu, Eds. (Elsevier, 1992), pp. 108–113.
19. B. Gludovatz *et al.*, *Science* **345**, 1153–1158 (2014).
20. J. W. Yeh *et al.*, *Adv. Eng. Mater.* **6**, 299–303 (2004).
21. M. Takeyama, C. T. Liu, *J. Mater. Res.* **3**, 665–674 (1988).
22. C. T. Liu, E. P. George, W. C. Oliver, *Intermetallics* **4**, 77–83 (1996).
23. T. Takasugi, C. Ma, S. Hanada, *Mater. Sci. Eng. A* **192–193**, 407–412 (1995).
24. T. Takasugi, O. Izumi, *Acta Metall.* **33**, 1247–1258 (1985).
25. M. Matsuda *et al.*, *J. Mater. Sci.* **46**, 4221–4227 (2011).
26. C. G. McKamey, J. A. Horton, C. T. Liu, *J. Mater. Res.* **4**, 1156–1163 (1989).
27. D.-M. Wee, T. Suzuki, *Trans. Japan Inst. Metals* **20**, 634–646 (1979).
28. R. Sundar, T. Kutty, D. Sastry, *Intermetallics* **8**, 427–437 (2000).
29. S. Chen *et al.*, *J. Alloys Compd.* **795**, 19–26 (2019).
30. W. H. Liu, Y. Wu, J. Y. He, T. G. Nieh, Z. P. Lu, *Scr. Mater.* **68**, 526–529 (2013).
31. T. Takasugi, O. Izumi, *Acta Metall.* **33**, 49–58 (1985).
32. B. Zhou, Y. T. Chou, C. T. Liu, *Intermetallics* **1**, 217–225 (1993).
33. O. I. Gorbatov *et al.*, *Phys. Rev. B* **93**, 224106 (2016).
34. R. Sun, C. Woodward, A. van de Walle, *Phys. Rev. B* **95**, 214121 (2017).
35. K. J. Hemker, M. J. Mills, *Philos. Mag. A* **68**, 305–324 (1993).
36. D. Crudden, A. Mottura, N. Warnken, B. Raeisinia, R. Reed, *Acta Mater.* **75**, 356–370 (2014).
37. A. Goodfellow *et al.*, *Acta Mater.* **153**, 290–302 (2018).
38. J. Douin, P. Veyssière, P. Beauchamp, *Philos. Mag. A* **54**, 375–393 (1986).
39. E. Schulson, Y. Xu, P. Munroe, S. Guha, I. Baker, *Acta Metall. Mater.* **39**, 2971–2975 (1991).
40. S.-J. Liang, D. Pope, *Acta Metall.* **25**, 485–493 (1977).
41. I. Baker, B. Huang, E. Schulson, *Acta Metall.* **36**, 493–499 (1988).
42. D. Muller, S. Subramanian, P. Batson, J. Silcox, S. Sass, *Acta Mater.* **44**, 1637–1645 (1996).
43. M. J. Mills, *Scr. Metall.* **23**, 2061–2066 (1989).
44. J. E. Hack, D. J. Srolovitz, S. P. Chen, *Scr. Metall.* **20**, 1699–1704 (1986).
45. P. M. Anderson, J. Rice, *Scr. Metall.* **20**, 1467–1472 (1986).
46. J. Hu, Y. N. Shi, X. Sauvage, G. Sha, K. Lu, *Science* **355**, 1292–1296 (2017).
47. T. Chookajorn, H. A. Murdoch, C. A. Schuh, *Science* **337**, 951–954 (2012).
48. C. C. Koch, R. O. Scattergood, M. Saber, H. Kotan, *J. Mater. Res.* **28**, 1785–1791 (2013).
49. C. C. Koch, R. O. Scattergood, K. A. Darling, J. E. Semones, *J. Mater. Sci.* **43**, 7264–7272 (2008).

ACKNOWLEDGMENTS

Funding: The authors from City University of Hong Kong (CityU) are grateful for the financial support from the Hong Kong Research Grant Council (RGC) with CityU (grants 11213319, 11202718, and 9360161). C.Y.Y. acknowledges financial support from the National Natural Science Foundation of China (no. 51701125) and the Natural Science Foundation of Shenzhen University (no. 827-000180). The authors from the Hong Kong Polytechnic University (PolyU) are grateful for the financial support from the Hong Kong RGC (25202719) and the National Natural Science Foundation of China (NSFC 51801169). **Author contributions:** C.T.L. and T.Y. designed the research. T.Y. and Y.L.Z. prepared and characterized the samples. Y.L.Z., J.H.L., and W.P.L. conducted the TEM, 3D-APT, and TEM-EDX analyses, respectively. C.Y.Y. and D.Y.L. carried out the DFT simulations. L.F. and Z.B.J. conducted the hot-hardness tests. T.Y., Y.L.Z., W.P.L., J.H.L., J.J.K., X.J.L., W.H.L., J.C.H., and C.T.L. analyzed the data and discussed the results. T.Y., Y.L.Z., J.J.K., and C.T.L. wrote the manuscript. All authors reviewed and contributed to the final manuscript. **Competing interests:** The authors declare no conflict of interest. **Data and materials availability:** All data are available in the main text or the supplementary materials.

SUPPLEMENTARY MATERIALS

science.sciencemag.org/content/369/6502/427/suppl/DC1
Materials and Methods
Figs. S1 to S11
Tables S1 and S2

11 March 2020; accepted 8 June 2020
10.1126/science.abb6830